HAL
open science

Micrometric Monodisperse Solid Foams as Complete Photonic Bandgap Materials

Ilham Maimouni, Maryam Morvaridi, Maria Russo, Gianluc Lui, Konstantin Morozov, Janine Cossy, Marian Florescu, Matthieu Labousse, Patrick Tabeling

▶ **To cite this version:**

Ilham Maimouni, Maryam Morvaridi, Maria Russo, Gianluc Lui, Konstantin Morozov, et al.. Micrometric Monodisperse Solid Foams as Complete Photonic Bandgap Materials. ACS Applied Materials & Interfaces, 2020, 10.1021/acsami.0c04031 . hal-02892582

HAL Id: hal-02892582

https://hal.science/hal-02892582v1

Submitted on 7 Jul 2020

HAL is a multi-disciplinary open access archive for the deposit and dissemination of scientific research documents, whether they are published or not. The documents may come from teaching and research institutions in France or abroad, or from public or private research centers.

L'archive ouverte pluridisciplinaire **HAL**, est destinée au dépôt et à la diffusion de documents scientifiques de niveau recherche, publiés ou non, émanant des établissements d'enseignement et de recherche français ou étrangers, des laboratoires publics ou privés.

Micrometric Monodisperse Solid Foams as Complete Photonic Bandgap Materials

Ilham Maimouni†[1], Maryam Morvaridi†[1], Maria Russo†[1,4], Gianluc Lui[2], Konstantin Morozov[3], Janine Cossy[4], Marian Florescu[2], Matthieu Labousse*[5], Patrick Tabeling[1]

[1]*Microfluidique, MEMS et Nanostructures, Institut Pierre-Gilles de Gennes, CNRS UMR 8231, ESPCI Paris and Paris Sciences et Lettres (PSL) Research University, 75005 Paris, France.*
[2]*Advanced Technology Institute and Department of Physics, University of Surrey, Guildford, Surrey GU2 7XH, United Kingdom*
[3]*Department of Chemical Engineering Technion – Israel Institute of Technology Haifa 320000, Israel*
[4]*Molecular, Macromolecular Chemistry and Materials, ESPCI Paris, CNRS, PSL University, 10 Rue Vauquelin, 75231 Paris Cedex 5, France*
[5]*Gulliver, CNRS UMR 7083, ESPCI Paris and Paris Sciences et Lettres (PSL) Research University, 75005 Paris France.*

†These authors equally contributed.

Corresponding author: matthieu.labousse@espci.psl.eu

KEYWORDS 3D solid foams, self-assembly, microfluidics, polymers, photonic band gaps

ABSTRACT: Solid foams with micrometric pores are used in different fields (filtering, 3D cell culture, etc.), but today, controlling their foam geometry at the pore level, their internal structure, and the monodispersity, along with their mechanical properties, is still a challenge. Existing attempts to create such foams suffer either from slow speed or size limitations (above 80 µm). In this work, by using a temperature-regulated microfluidic process, 3D solid foams with highly monodisperse open pores (PDI lower than 5%), with sizes ranging from 5 to 400 µm and stiffnesses spanning 2 orders of magnitude, are created for the first time. These features open the way for exciting applications, in cell culture, filtering, optics, etc. Here, the focus is set on photonics. Numerically, these foams are shown to open a 3D complete photonic bandgap, with a critical index of 2.80, thus compatible with the use of rutile TiO_2. In the field of photonics, such structures represent the first physically realizable self-assembled FCC (face-centered cubic) structure that possesses this functionality.

INTRODUCTION

Solid polymer foams are widely used in a variety of fields such as insulation, packaging, electronic and biomedical applications.[1,2] Indeed, they combine the remarkable features of liquid foams in terms of lightness, high surface area, tunable porosity and topological organization with interesting stiffness properties. Depending on the application, the required structural properties vary, especially the pore size and the wall thickness, which makes the fabrication process critical. Different conventional and advanced processing techniques have been developed to obtain such structures with customized properties.[3] However, none of them succeeded in downscaling the foam pore size to few micrometers, while keeping control over the pore size and the stiffness, which dramatically limits their potential. All existing methods of 3D solid polymer foam fabrication generate strong inhomogeneity when targeting foams with pore sizes smaller than 80 µm.[4] Although adequate for a range of applications, this polydispersity becomes detrimental when highly controlled structures are needed. Different domains such as photonics, 3D cell culture, or filtering would considerably benefit from the availability of solid foams with highly tunable monodisperse pores of few micrometers. For example, for 3D cell cultures embedded within a solid polymer foam, it would be advantageous to cover a large range of micrometric pore sizes in a way that matches the diversity of cells dimensions.[1, 3, 5]

Recently, 2D foams with controlled pore size distribution[6] have been demonstrated to exhibit outstanding photonic properties, hence raising the possibility of employing 3D solid polymer foams as templates for Photonic Band Gap (PBG) materials.[7-18] Such materials prevent the propagation of electromagnetic waves in a frequency range called a band gap. The fabrication of polymer based photonic materials[10, 19-26] in the near infrared and the visible range has been developed.[27] Among the explored configurations, rod-connected lattices[28, 29] showed the best photonic performances. They exhibited a full PBG at lower refractive index,[30] enlarging the width of PBG for refractive index of 3.6[31] and getting higher mid-gap center frequency. Such rod-connected lattices are a feature of 3D open cell foams where plateau borders self-assemble into well-organized structures.[32] However, even though the photonic diamond network was introduced almost 30 years ago[28] and despite decades of active research in the field, [33-36] the physical realization of self-assembled photonic structure with a complete photonic band gap remains elusive.

In this article, we explore physically realizable 3D polymer solid foams as a new potential class of PBG materials that can be accurately self-assembled and downscaled by using

microfluidics, without increasing the complexity of the unit cell structure. To produce 3D solid foams with tunable properties, microfluidics, combined with liquid templating routes, has already tentatively been used.[37-40] In References [4, 37-40], monodisperse solid foams were obtained by using a Flow Focusing (FF) microfluidic device, and cross-linking the polymer aqueous solutions to solidify the material. However, solidification-induced clogging issues prevented from obtaining monodisperse solid foams with pores smaller than 80 µm.[4] In the present work, we solve this problem by developing a temperature-regulated microfluidic process to tune the solidification along the fabrication process. Consequently, monodisperse solid foams with a Polydispersity index (PDI) less than 10 %, covering a pore size range from 5 µm to 400 µm, and with stiffnesses spanning 2 orders of magnitude were obtained.

Here, we uncover an outstanding photonic potential of these foams. We numerically show that 3D solid FCC (Face-centered cubic, Kepler structure) foams, explored for the first time here, exhibit 3D complete photonic band gaps in a range of refractive index compatible with existing materials, a property that previous self-assembled structures were unable to match. Our work thus opens a new route for fabricating self-assembled complete photonic band gap materials.

RESULTS AND DISCUSSION

Figure 1a shows the Flow Focusing microfluidic device used to produce the solid polymer foams discussed here (see Supporting Information, SI1). First, a liquid polymer foam is generated at low temperature (10°C), using gas volume fractions above the jamming point.[41] In such conditions, bubbles self-assemble in monodisperse and ordered patterns (inset, Figure 1a). The resulting liquid polymer foam is spread over a glass plate and then exposed to a temperature of 70 °C. This step toughens the structure, thus avoiding the formation of heterogeneity induced by liquid foam aging. The process forms a few (2-3) bubbles layer foam. It can be repeated several times to obtain a thicker solid foam (see Supporting information, SI3). Following this procedure and using one microfluidic generator (one nozzle), a crosslinked foam sample of 2 cm^3 (with pore sizes = 100 µm) can be produced in 1 hour. The parallelization of 5-10 microfluidic chips would allow us to multiply the produced volume accordingly. The obtained monodisperse foams are locally ordered (Figure 1b) and, in agreement with the literature, organize into two stable crystalline structures depending on the filling fraction. At high filling fraction (wet state) the system self-organizes into a Face-Centered Cubic Structure (FCC, Kepler structure) while at low filling fraction (dry state), the foam is a Body-Centered Cubic structure (BCC, Kelvin structure).[42] As shown in Figure 1c and 1d, for a filling fraction φ above 9% a FCC-like structure is observed (Figure 1c, φ=11%), whereas for 5% < φ < 9% (Figure 1d, φ=8%), a transition between the dry and the wet states occurs and a coexistence of BCC and FCC structures is obtained; finally, for φ < 5%, BCC-like structures are obtained.[40, 43]

The pore sizes of the 3D solid foams are varied by adjusting the channel dimensions (see Supporting Information, SI1), flow pressures and reactant concentrations. Figure 2a-d show confocal transmission images of 3D solid foams with a pore size ranging from 400 µm down to 5 µm. All the designed foams pores size distributions follow a normal distribution with polydispersity indices (i.e. normalized size standard deviation) of few percent (2% in Figure 2e). Figure 2f-h, show SEM images of 3D chitosan solid foam with different layers of interconnected open pores ranging from 100µm to 5 µm. The films separating the bubbles completely disappear during the foam preparation, so that the gas phase percolate withing the structure, making the structure suitable for the photonic application. Indeed, closed cell foams do not open any PBG (see Supporting Information, SI9). The mechanical behavior of foam samples (e.g. Figure 2i) at different cross-linker concentrations under compression is showed in Figure 2j. As commonly observed with foams, different regions can be individuated in the curves[44] (Figure 2j). In order to estimate the elastic modulus *E*, the elastic region at low strain is taken into consideration. Results show that the elastic modulus *E* spans a range of two orders of magnitude (respectively from about 10^3 to 10^5 *Pa* in Fig. 2j), by increasing the amount of cross-linker. Consequently, it is noteworthy that the described microfluidic process allows a tuning of the mechanical properties, which can be necessary for material handling and manipulation as in photonic devices. The access to a material with a large range of elasticities is crucial for other applications where the mechanical behavior is a main functionality like in 3D cell culture for tissue engineering.[5]

The structures in the confocal images of Figure 1 and 2 are composed of ordered layers in the out-of-plane direction of depths typically larger than 4-5 layers, a number above the evanescent penetration depth (3.2 layers, see Experimental Section). Consequently, we infer that the electromagnetic field vanishes out in the band gap within the first encountered layers. The obtained solid structure shares the topological and geometric features of the original liquid foam template: the Plateau Borders (PB) thicken in the close vicinity of the nodes but are of a constant diameter in most of the central region, i.e. on two-third of the PB length ±15% (see Supporting Information, SI4).

To fully explore the potential of the fabricated foams for photonic applications, we simulate the electromagnetic response in foam configurations. Guided by the experiments, we restricted ourselves to the study of observed structures, i.e. Kelvin and Kepler foams. Indeed, another interesting structure called Weaire-Phelan foam and that is more energetically favorable,[43,45] exhibits a significantly wide complete photonic bandgap.[33-36] However, from an experimental prospective and contrarily to Kelvin and Kepler structures, this foam does not form spontaneously and needs a forcing to exist. This feature raises serious experimental challenges for its fabrication.[46] The Kelvin structure also presents a photonic bandgap but it has rather limited width.[33] The band structure of Kepler foam remains unknown. We model Kepler (FCC) and Kelvin (BCC) structures by networks of connected rods of diameter d and relative dielectric constant ϵ embedded within a unit cell of size a. The remaining volume is occupied by air of relative

dielectric constant $\epsilon_{\text{air}} = 1$ (see Supporting Information, SI6). We numerically investigate the optical properties of the two structures represented in Figure 3a and 3c. The band structure is found by numerically solving Maxwell's equations through finite-element eigenmode decomposition with periodic boundary conditions[47] and with the spectral MPB method,[48] two approaches that are found in excellent agreement (see Supporting Information, SI6). We investigate the band structure as a function of the dimensionless frequency $f = \omega a/(2\pi c)$ with ω the frequency and c the speed of light. The band diagram of the FCC structure in Figure 3b shows the presence of a complete band gap with a gap-midgap $\%\text{BG} = \frac{\text{band width}}{\text{mean f in the BG}} = 8.95$. Similarly, we numerically compute the band structure of the BCC structure and observe, as shown in Figure 3d, a complete BG opening, with $\%\text{BG} = 3.35$. The crossing of bands in Figure 3b and 3d indicates a triple degeneracy at the points of the Brillouin zone which is expected as a natural consequence of the three four-fold rotational symmetry of the unit cell.[49] Notably, for both structures, the band gap does not close along the standard paths of the Brillouin zone (upper edges of the band gap occur along edges of the irreducible Brillouin zone), a result that has been confirmed by Density of States (DOS) calculations (see Supporting information, SI8). Furthermore, we find no significant influence of the rods and the vertices geometries on the bandgap width, we pursue our numerical investigation modeling foam Plateau borders as cylindrical rods (see Supporting Information, SI10). We numerically explore in Figure 4a the dependence of the gap-midgap ratio on the geometrical and optical parameters of the unit cell. Maxwell's equations are scale invariant so that the band gap depends only on the dimensionless rod's diameter $\tilde{d}=d/a$ and on the optical index $n = \sqrt{\varepsilon}$ of the rods. For a given rod optical index, we vary the rod diameter and measure the corresponding %BG. For both structures we observe that above a critical index a large band gap opens for a pronounced range of rod diameter. In both structures, an optimal rod diameter is found as a function of its optical index. We also note that for a given index, the %BG is always larger for an FCC structure than for a BCC structure. Figure 4a shows an increase in %BG with the optical index and more importantly a critical optical index (n^*) below which the band gap closes. In Figure 4b we investigate the evolution of the maximum %BG with the rods index for both the FCC and BCC structures. The %BG increases with the optical index and a critical index threshold is evidenced $n^* = 2.80$ for FCC and $n^* = 3.21$ for BCC. It is noteworthy recalling that large optical index contrasts are usually required to open band gaps. For example, for the inverse opal structure,[50] a band gap opens for an optical index contrast larger than 2.92. In contrast, Figure 4b shows that FCC solid foam exhibits a critical index $n^* = 2.80$ which makes it possible, for the first time, to open a band gap using the rutile TiO_2 for example ($n = 2.9$), a key result of this investigation. The mechanism of the band gap opening can be rationalized by exploring the spatial distribution of the field mode intensity of the dielectric and the air band,[49] the band respectively below and above the gap. For the air band, the field intensity is concentrated into region of small dielectric constant. Conversely, for the dielectric band the field intensity is concentrated into region of large dielectric constant. This field concentration into different dielectric areas is driven by the dielectric contrast between these two areas. Therefore, for large dielectric contrast the coexistence of the dielectric and air bands is precluded in the frequency domain and a band gap opens (see Supporting Information, SI7).[49] Coincidentally and in striking contrast with the BCC phase, the FCC structure combines all possible advantages: it is obtained in a pure configuration (Figure 1c), it exhibits larger PBG (Figure 3b), which occurs at a lower critical optical index contrast (Figure 4b).

Conclusion

To conclude, we have successfully fabricated unprecedented highly monodisperse 3D solid foams, in the micrometric range (pore size 5-400 µm). These foams can be used as templates for complete photonic band gaps structures. The temperature-regulated microfluidic approach used to fabricate these solid foams solves the fabrication issues that thus far prevented their miniaturization. These new physically realizable structures that display photonic band gaps for an index contrast of 2.80 represent a substantial progress in the field of self-assembled photonic band gap materials. These foams open up numerous applications in the infrared (IR) domain where they can be used as templates for cooling materials (blocking infrared radiations) in the building industry or as angle-independent LiDAR filters for autonomous vehicles in the mass automotive market. The IR domain is highly demanding for new innovations and remains more accessible than the "visible" market saturated by well-established silicon-based technologies.

Still, the obtained solid foams could be further downscaled by combining the process described here with the standard downscaling methods existing for liquid emulsions.[51] This task is achievable with lithography techniques and can be facilitated by using step-emulsification configuration, which produces submicron droplets with high throughput. Bubbles of 400 nm would lead to a band gap centered on 500 nm, as mentioned above. At this wavelength, the refractive index of rutile TiO_2 is close to 2.9. Therefore, the foam template will have to be coated with high refractive index materials using dip-coating or physical vapor deposition techniques like sputtering. This has been tentatively explored and preliminary results are showed in Supporting Information, SI5. Otherwise, the polymer forming the 3D foam template will have to be substituted by rutile TiO_2, a process finely reported by Muller et al..[52] These numbers indicate that our foam technology has a serious potential to create a complete PBG material in the visible range.

Although we focused on its photonic band gap, the interest for the proposed micrometric foams is not restricted to this domain. The access to 3D solid polymer foams with a high tunability in terms of pore size and mechanical properties opens other applications such as 3D cell culture for tissue engineering and regenerative medicine.

EXPERIMENTAL SECTION

Foam fabrication process. Monodisperse liquid foam generation is carried out in a Flow Focusing microfluidic geometry (Figure 1a). The device is made by standard soft photolithography and replica-molding techniques using polydimethylsiloxane (PDMS). The channels have a depth of 5-50 µm and a width of 5-400 µm depending on the desired pore size (see Supporting Information, SI1). The setup contains two inlets for injecting the liquid and the gas phases respectively through plastic tubes, and an outlet tube for foam collection. The gas phase is nitrogen with traces of perfluorohexane C_6F_{14} in order to hinder Ostwald ripening.[38] The liquid phase is an aqueous solution of chitosan (Mw = $0.3 \cdot 10^6$ g/mol, Sigma Aldrich), a biopolymer extracted from shrimp shells, at a concentration varying between 0.3 and 1 %w/v in milliQ water. Acetic acid is added to the solution at a concentration of 0.1 mol/L. Lutensol AT25 (provided by BASF), a non-ionic surfactant, is added at a concentration of 4 g/L. The surfactant permits stabilization of the liquid/air interface. Dissolution and homogenization are obtained by stirring for at least 2 days at room temperature. The crosslinking agent Glyoxal (40% in water, purchased from Sigma Aldrich) is added at low temperature to the liquid phase at a concentration varying between 2 and 50 %v/v. The obtained liquid phase is kept in an ice bath in order to prevent the crosslinking.

At the nozzle where the gas phase meets the liquid phase, micro-bubbles of gas are encapsulated in the continuous liquid phase. A bubble generation frequency between 400-800 bubbles per second is obtained depending on the gas and liquid pressures. The flows are pressure-driven at a pressure p_{gas} and p_{liq} (0.05 - 5 bar) using a MFCS™-EZ pressure controller system (Fluigent) connected to a nitrogen tap. The temperature of the microfluidic chip is fixed at 5-10 °C using a Peltier device in order to prevent crosslinking inside the microfluidic chip. The thus obtained liquid foam layer can then be heated at a temperature between 50 and 100 °C, thus above the chitosan crosslinking temperature (40 °C)[53] for 1-5 minutes. For the samples presented here, the temperature was set at 70 °C. For a thin sample (under 1-3 mm in height), the crosslinking takes 2-3 min. For larger samples, a layer-by-layer procedure is followed (see Supporting Information, SI2 and SI3). The in-situ foam generation is tracked using an Optical Microscope (Leica) with 4-20x scanning objectives.

Morphological characterization. To characterize the solid foam morphology, the sample is placed on a microscope glass slide and images are taken using Optical and Confocal microscope systems (Leica) taking advantage of the auto-fluorescence of chitosan (in green). For confirmation, the morphological characteristics of the solid foams were also checked using Scanning Electron Microscope (SEM, FEI Magellan400 at 5-10 kV). Images are analyzed by using a Matlab code that allows studying the topology of the foam (pore size distribution, PB profile in Supporting Information, SI4).

Mechanical characterization. In order to determine the elastic modulus of the fabricated foams, compression tests are performed on different solid chitosan foams samples containing different concentrations of cross-linker (from 100 to 400 µL of Glyoxal in 1 mL of chitosan solution at 0.6%wt). An Instron 5865 universal testing machine with a 500 N load cell is used. The compression rate is 10 mm/min. Each test is conducted three times. The elastic modulus E is calculated as the slope of the linear elastic region (at low strain, under 15%) in the stress-strain curves.

Photonic band gap simulation. Band structure and photonic eigenmode are calculated using spectral methods with a planewave basis (MPB software package).[48] We employ a 128x128x128 spatial mesh and a corresponding planewave basis consisting ~2×10^6 k-vectors, which ensures full convergence of the band structure calculation results. The band structure calculation results shown above are fully confirmed through finite element package Comsol Multiphysics (ver.5.4) (see Supporting Information, SI6).

Estimation of the penetration depth of the FCC structure in the band gap. At the bottom of the air band the penetration depth[(23)] $\delta \simeq \left(\frac{\alpha}{\Delta f}\right)^{-1/2}$ with $\alpha = \frac{\partial^2 f}{\partial k^2}$ the local curvature along a given wave vector path and $\Delta f \simeq 5 \cdot 10^{-2}$ corresponding to half of the bandgap width. The bottom of the air band occurs along the wave vector path Γ-K and we estimate $\delta \simeq 3.2 \pm 0.1$ [unit cell].

SUPPORTING INFORMATION

Supporting Information is available free of charge on the ACS Publications website at DOI: xxx

- Geometrical characteristics of the used microfluidic devices; Crosslinking methods and layer-by-layer solidification process for foam sample; Plateau Border thickness profile analysis; Coating of the 3D solid polymer structure; Band diagram using *Comsol Multiphysics*; Numerical field distribution analysis; Density of States Calculations; Band diagram for closed cell foam; Distorted Network Decorations.

AUTHOR INFORMATION

Corresponding Author

* matthieu.labousse@espci.psl.eu

Author Contributions

IM, MR carried out the experimental work; MM, GL performed the simulations; JC contributed in the synthesis of materials; KM contributed to the research; IM, MM, MR, GL, MF, ML, PT interpreted the results; MF, ML, PT supervised the research project; IM, MR, MF, ML, PT prepared the manuscript. IM, MM, MR contributed equally to this work.

ACKNOWLEDGMENTS

The authors warmly thank Z. Amara, L. Berthier, R. Carminati, C.M. Cejas, P. Chaikin, W. Drenckhan, A. Leshansky, D. Pine, S. Torquato, E. Yablonovitch for enlightening discussions; J. Bico for the help with the mechanical tests; MMN group for experimental insights, ESPCI, CNRS, IPGG. M.F. acknowledges support from

EPSRC (United Kingdom) Strategic Equipment Grant No. EP/L02263X/1 (EP/M008576/1) and EPSRC (United Kingdom) Grant EP/M027791/1. Authors acknowledge supports from MICROFLUSA (funded by the European Union Horizon 2020 research and innovation programme under Grant Agreement No. 664823).

DATA AVAILIBILITY

The data underlying the findings of this study are available without restriction.[54]

REFERENCES

1. Netti PA. Biomedical Foams for Tissue Engineering Applications: Elsevier; 2014.
2. Mills N. Polymer Foams Handbook: Engineering and Biomechanics Applications and Design Guide: Elsevier; 2007.
3. Maimouni I, Cejas CM, Cossy J, Tabeling P, Russo M. Microfluidics Mediated Production of Foams for Biomedical Applications. Micromachines. 2020;11(1):83.
4. Andrieux S, Quell A, Stubenrauch C, Drenckhan W. Liquid Foam Templating–A Route to Tailor-Made Polymer Foams. Advances in Colloid and Interface Science. 2018;256:276-290.
5. Engler AJ, Sen S, Sweeney HL, Discher DE. Matrix Elasticity Directs Stem Cell Lineage Specification. Cell. 2006;126(4):677-689.
6. Ricouvier J, Tabeling P, Yazhgur P. Foam as a Self-Assembling Amorphous Photonic Band Gap Material. Proceedings of the National Academy of Sciences. 2019;116(19):9202-9207.
7. Yablonovitch E, Gmitter T, Meade R, Rappe A, Brommer K, Joannopoulos J. Donor and Acceptor Modes in Photonic Band Structure. Physical Review Letters. 1991;67(24):3380.
8. Miguez H, Chomski E, García- Santamaría F, Ibisate M, John S, López C, Meseguer F, Mondia JP, Ozin GA, Toader O, van Drielet, HM. Photonic Bandgap Engineering In Germanium Inverse Opals by Chemical Vapor Deposition. Advanced Materials. 2001;13(21):1634-1637.
9. Wang Y, Li W, Li M, Zhao S, De Ferrari F, Liscidini M, Omenetto FG. Biomaterial- Based "Structured Opals" with Programmable Combination of Diffractive Optical Elements and Photonic Bandgap Effects. Advanced Materials. 2019;31(5):1805312.
10. Noda S, Tomoda K, Yamamoto N, Chutinan A. Full Three-Dimensional Photonic Bandgap Crystals at Near-Infrared Wavelengths. Science. 2000;289(5479):604-606.
11. Fleming J, Lin S, El-Kady I, Biswas R, Ho K. All-Metallic Three-Dimensional Photonic Crystals with Large Infrared Bandgap. Nature. 2002;417(6884):52.
12. Kosaka H, Kawashima T, Tomita A, Notomi M, Tamamura T, Sato T, Kawakami S. Superprism Phenomena in Photonic Crystals: Toward Microscale Lightwave Circuits. Journal Of Lightwave Technology. 1999;17(11):2032-2038.
13. López C. Materials Aspects of Photonic Crystals. Advanced Materials. 2003;15(20):1679-1704.
14. Ritari T, Tuominen J, Ludvigsen H, Petersen J, Sørensen T, Hansen TP, Simonsen HR. Gas Sensing using Air-Guiding Photonic Bandgap Fibers. Optics Express. 2004;12(17):4080-4087.
15. Akahane Y, Asano T, Song B-S, Noda S. Fine-Tuned High-Q Photonic-Crystal Nanocavity. Optics Express. 2005;13(4):1202-1214.
16. Fujita M, Ueno T, Ishihara K, Asano T, Noda S, Ohata H, Tsuji T, Nakada H, Shimoji N. Reduction of Operating Voltage in Organic Light-Emitting Diode by Corrugated Photonic Crystal Structure. Applied physics letters. 2004;85(23):5769-5771.
17. Wu L, Wang W, Zhang W, Su H, Gu J, Liu Q, Zhang D, Pantelić D, Jelenković B. Optical Performance Study of Gyroid- Structured TiO2 Photonic Crystals Replicated from Natural Templates using a Sol- Gel Method. Advanced Optical Materials. 2018;6(21):1800064.
18. Peng S, Zhang R, Chen VH, Khabiboulline ET, Braun P, Atwater HA. Three-Dimensional Single Gyroid Photonic Crystals with a Mid-Infrared Bandgap. ACS Photonics. 2016;3(6):1131-1137.
19. Blanco A, Chomski E, Grabtchak S, Ibisate M, John S, Leonard SW, Lopez C, Meseguer F, Miguez H, Mondia JP, Ozin GA, Toader O, van Driel HM. Large-Scale Synthesis of a Silicon Photonic Crystal with a Complete Three-Dimensional Bandgap Near 1.5 Micrometres. Nature. 2000;405(6785):437-440.
20. Straub M, Gu M. Near-infrared Photonic Crystals with Higher-order Bandgaps Generated by Two-photon Photopolymerization. Optics letters. 2002;27(20):1824-1826.
21. Serbin J, Gu M. Experimental Evidence for Superprism Effects in Three- Dimensional Polymer Photonic Crystals. Advanced materials. 2006;18(2):221-224.
22. Tétreault N, von Freymann G, Deubel M, Hermatschweiler M, Pérez- Willard F, John S, Wegener M, Ozon GA. New Route to Three- Dimensional Photonic Bandgap Materials: Silicon Double Inversion of Polymer Templates. Advanced Materials. 2006;18(4):457-460.
23. Thiel M, Decker M, Deubel M, Wegener M, Linden S, von Freymann G. Polarization Stop Bands in Chiral Polymeric Three- Dimensional Photonic Crystals. Advanced Materials. 2007;19(2):207-210.
24. Staude I, Thiel M, Essig S, Wolff C, Busch K, Von Freymann G, Wegener M. Fabrication and Characterization of Silicon Woodpile Photonic Crystals with a Complete Bandgap at Telecom Wavelengths. Optics letters. 2010;35(7):1094-1096.
25. Chen L, Taverne MP, Zheng X, Lin J-D, Oulton R, Lopez-Garcia M, D Ho Y-L, Rarity JR. Evidence of Near-Infrared Partial Photonic Bandgap in Polymeric Rod-Connected Diamond Structures. Optics express. 2015;23(20):26565-26575.
26. Wong S, Deubel M, Pérez- Willard F, John S, Ozin GA, Wegener M, von Freymann G. Direct Laser Writing of Three- Dimensional Photonic Crystals with a Complete Photonic Bandgap in Chalcogenide Glasses. Advanced Materials. 2006;18(3):265-269.
27. Frölich A, Fischer J, Wolff C, Busch K, Wegener M. Frequency- Resolved Reciprocal- Space Mapping of Visible Spontaneous Emission from 3D Photonic Crystals. Advanced Optical Materials. 2014;2(9):849-853.
28. Chan C, Ho K, Soukoulis C. Photonic Band Gaps in Experimentally Realizable Periodic Dielectric Structures. EPL (Europhysics Letters). 1991;16(6):563.
29. Maldovan M, Thomas EL. Diamond-Structured Photonic Crystals. Nature Materials. 2004;3(9):593-600.
30. Men H, Lee KY, Freund RM, Peraire J, Johnson SG. Robust Topology Optimization of Three-Dimensional Photonic-Crystal Band-Gap Structures. Optics express. 2014;22(19):22632-22648.

31. Kee C-S, Han S-P, Yoon KB, Choi C-G, Sung HK, Oh SS, Hae Yong P, Sunggook P, Helmut S. Photonic Band Gaps and Defect Modes of Polymer Photonic Crystal Slabs. Applied Physics Letters. 2005;86(5):051101.
32. Weaire DL, Hutzler S. The Physics of Foams. Oxford University Press; 2001.
33. Klatt MA, Steinhardt PJ, Torquato S. Phoamtonic Designs Yield Sizeable 3D Photonic Band Gaps. Proceedings of the National Academy of Sciences. 2019;116(47):23480-23486.
34. Adams GB, O'Keeffe M, Demkov AA, Sankey OF, Huang Y-M. Wide-Band-Gap Si in Open Fourfold-Coordinated Clathrate Structures. Physical Review B. 1994;49(12):8048.
35. Jung W, Kessens H, Ormeci A, Schnelle W, Burkhardt U, Borrmann H, Nguyen HD, Baitingera M, Grin Y. Synthesis, Crystal Structure and Physical Properties of the Clathrate-I Phase Ba 8 Rh x Si 46− x− y□ y. Dalton Transactions. 2012;41(45):13960-13968.
36. Dyachenko PN, Kundikova ND, Miklyaev YV. Band structure of a photonic crystal with the clathrate Si-34 lattice. Physical Review B. 2009;79(23):233102.
37. Andrieux Sb, Drenckhan W, Stubenrauch C. Generation of Solid Foams with Controlled Polydispersity Using Microfluidics. Langmuir. 2018;34(4):1581-1590.
38. Huerre A, Miralles V, Jullien M-C. Bubbles and Foams in Microfluidics. Soft Matter. 2014;10(36):6888-6902.
39. Testouri A. Highly Structured Polymer Foams from Liquid Foam Templates using Millifluidic Lab-On-A-Chip Techniques 2012.
40. Andrieux S, Drenckhan W, Stubenrauch C. Highly Ordered Biobased Scaffolds: from Liquid to Solid Foams. Polymer. 2017;126:425-431.
41. Forel E, Rio E, Schneider M, Beguin S, Weaire D, Hutzler S, Drenckhan W. The Surface Tells it All: Relationship Between Volume and Surface Fraction of Liquid Dispersions. Soft matter. 2016;12(38):8025-8029.
42. Drenckhan W, Hutzler S. Structure and Energy of Liquid Foams. Advances In Colloid And Interface Science. 2015;224:1-16.
43. Phelan R, Weaire D, Brakke K. Computation of Equilibrium Foam Structures using The Surface Evolver. Experimental Mathematics. 1995;4(3):181-192.
44. Chen F, Gällstedt M, Olsson R, Gedde U, Hedenqvist M. A Novel Chitosan/Wheat Gluten Biofoam Fabricated by Spontaneous Mixing and Vacuum-Drying. RSC Advances. 2015;5(114):94191-94200.
45. Weaire D, Phelan R. A Counter-Example to Kelvin's Conjecture on Minimal Surfaces. Philosophical Magazine Letters. 1994;69(2):107-110.
46. Gabbrielli R, Meagher AJ, Weaire D, Brakke KA, Hutzler S. An Experimental Realization of the Weaire–Phelan Structure in Monodisperse Liquid Foam. Philosophical Magazine Letters. 2012;92(1):1-6.
47. Morvaridi M, Carta G, Brun M. Platonic Crystal with Low-Frequency Locally-Resonant Spiral Structures: Wave Trapping, Transmission Amplification, Shielding and Edge Waves. Journal of the Mechanics and Physics of Solids. 2018;121:496-516.
48. Johnson SG, Joannopoulos JD. Block-Iterative Frequency-Domain Methods for Maxwell's Equations in a Planewave Basis. Optics express. 2001;8(3):173-190.
49. Joannopoulos JD, Johnson SG, Winn JN, Meade RD. Molding the Flow of Light. Princeton Univ Press, Princeton, NJ. 2008.
50. Vlasov YA, Bo X-Z, Sturm JC, Norris DJ. On-Chip Natural Assembly of Silicon Photonic Bandgap Crystals. Nature. 2001;414(6861):289.
51. Li Z, Leshansky A, Pismen L, Tabeling P. Step-Emulsification in a Microfluidic Device. Lab on a Chip. 2015;15(4):1023-1031.
52. Muller N, Haberko J, Marichy C, Scheffold F. Silicon Hyperuniform Disordered Photonic Materials with a Pronounced Gap in the Shortwave Infrared. Advanced Optical Materials. 2014;2(2):115-119.
53. Yang Q, Dou F, Liang B, Shen Q. Studies of Cross-Linking Reaction on Chitosan Fiber with Glyoxal. Carbohydrate Polymers. 2005;59(2):205-210.
54. Maimouni I, Morvaridi M, Russo M, Lui G, Morozov K, Cossy J, Florescu M, Labousse M, Tabeling P. Micrometric Monodisperse Solid Foams as Complete Photonic Bandgap Materials Figshare, https://doi.org/10.6084/m9.figshare.12444773 (2020)

Figures

Figure 1.

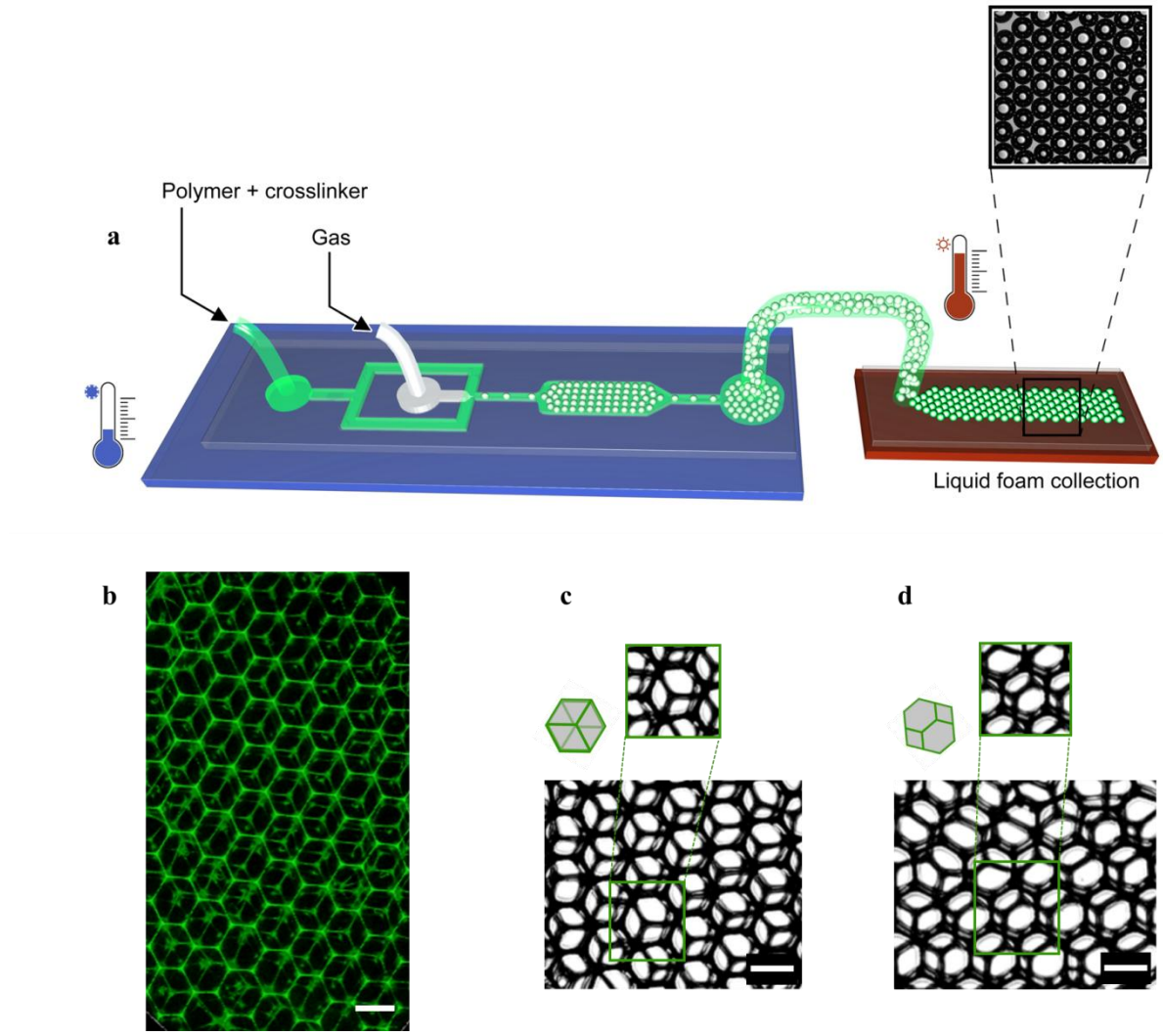

Figure 2

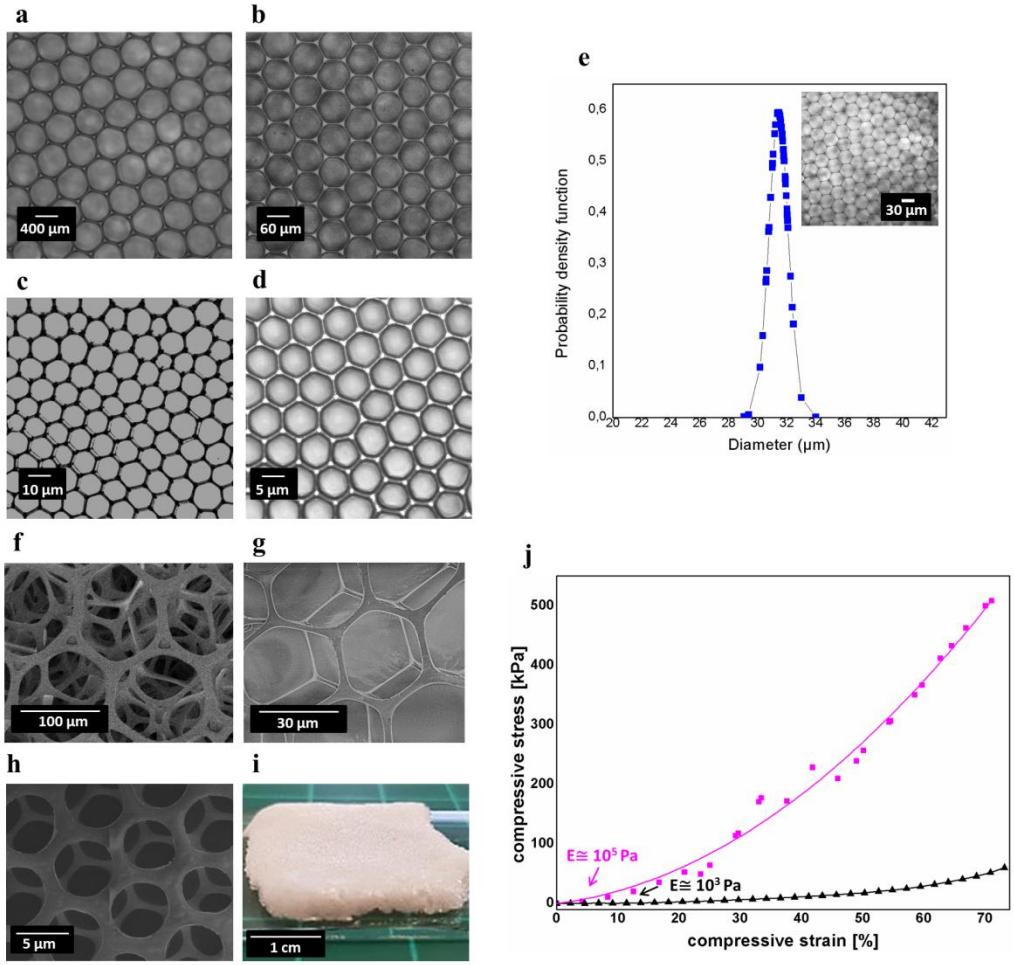
a
b
400 µm
60 µm
c
d
10 µm
5 µm
e
30 µm
Probability density function
Diameter (µm)
f
g
100 µm
30 µm
h
i
5 µm
1 cm
j
compressive stress [kPa]
compressive strain [%]
E≅ 10⁵ Pa
E≅ 10³ Pa

Figure 3.

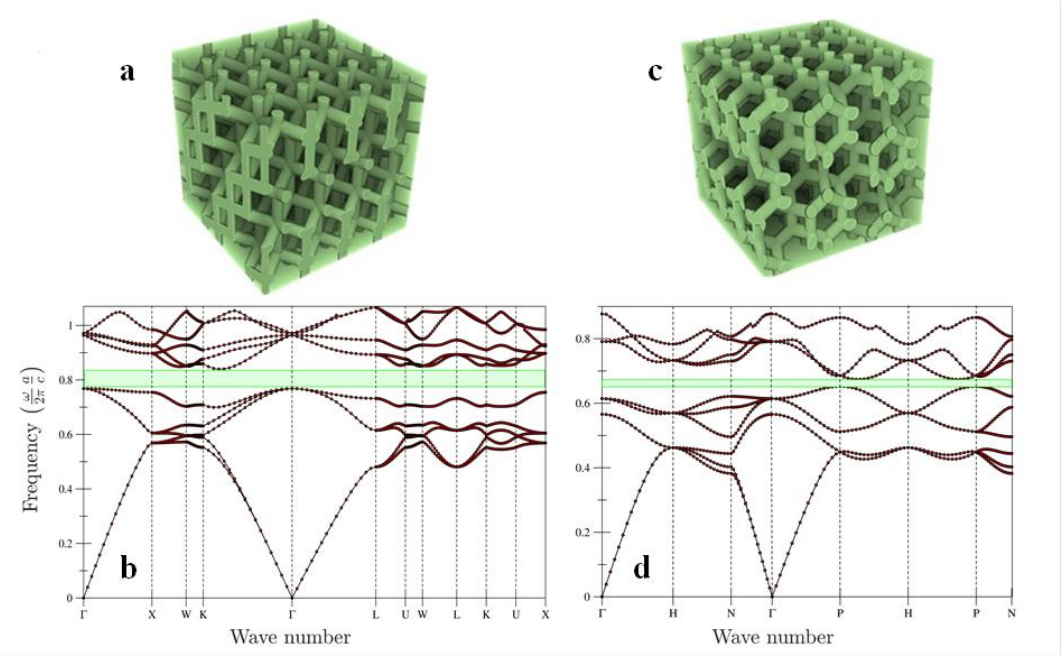
a
c
b
d
Frequency $\left(\frac{\omega}{2\pi}\frac{a}{c}\right)$
Wave number
Wave number
Γ X W K Γ L U W L K U X
Γ H N Γ P H P N

Figure 4.

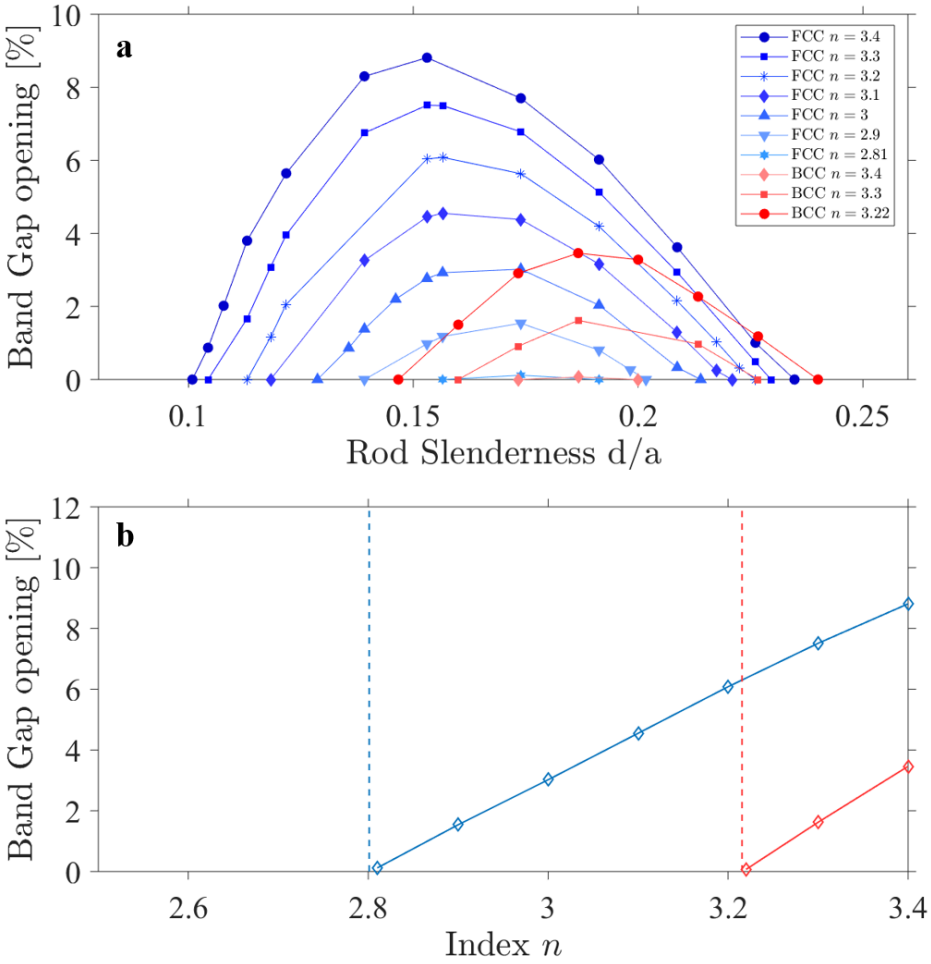
a
Band Gap opening [%]
Rod Slenderness d/a
FCC $n = 3.4$
FCC $n = 3.3$
FCC $n = 3.2$
FCC $n = 3.1$
FCC $n = 3$
FCC $n = 2.9$
FCC $n = 2.81$
BCC $n = 3.4$
BCC $n = 3.3$
BCC $n = 3.22$
b
Band Gap opening [%]
Index n

Figure 1. Experimental realization of tunable targeted foam structures. a Experimental sketch of the Flow Focusing platform producing liquid foams – Inset of a liquid wet foam picture with characteristic roundish bubbles. **b** a typical 3D confocal reconstruction of the produced highly ordered open-cell solid foam with slender Plateau Borders of uniform thickness. Scale bar 100 µm. **c** FCC chitosan solid foam (Filling fraction 11%, pore diameter: 20 µm, Plateau border thickness ~ 11µm). Scale bar 20 µm. **d** BCC solid foam crystal domain in a coexisting BBC-FCC phase. Filling fraction 8%, pore diameter: 20 µm, Plateau border thickness ~ 7µm). Scale bar 20 µm.

Figure 2. Experimental scaling down and mechanical properties of the solid foam. a-d Bright-field confocal images illustrating the pore size tuning between 400 µm and 5 µm with a narrow distribution. **e** The pores size distribution in **c** follows a Gaussian distribution, in the present case, centered around 31±0.6 µm (Polydispersity index 2%); **f, g, h** SEM images of 3D solid foams with pore size ranging from 100 µm to 5µm; **i** photograph of a typical prepared solid foam sample; **j** compressive stress-strain curves of the foam sample (pore size of 100 µm) for two different cross-linker concentrations: at 100µL of glyoxal (-▲-) and polynomial interpolation at 400µL of glyoxal (-■-) for 1 mL of chitosan at 0.6%wt.

Figure 3. Band structure calculations for the FCC and BCC structure. a (respectively **c**) Schematic representation of the FCC structure (resp. BCC structure). **b** (resp. **d**) Band structure calculations FCC (resp. BCC) for the optimal structure comprising cylinders of diameter d/a =0.153 (resp. d/a=0.202) corresponding to a filling ratio of 20.24% (resp. 20.94%), of relative dielectric constant $\epsilon = 11.56$ and a spatial mesh of 128x128x128. The structure displays a photonic band gap of 8.95% (resp. 3.35%) around a reduced central wave number a/λ=0.80 (resp. a/λ=0.66).

Figure 4. Optimal geometry for photonic band gap opening. a Numerical evolution of the gap-midgap ratio (%BG) with the dimensionless rod's diameter $\tilde{d} = d/a$. Red (resp. blue) colors refers to FCC (resp. BCC) structures. The darkening of the colors indicates larger optical indices n. **b** Numerical evolution of the geometrically optimal gap-midgap ratio (%BG) with the optical index of the rods. Vertical red (resp. blue) dashed line evidence the critical optical index $n^* = 2.80$ (resp. $n^* = 3.21$) to open a band in the FCC (resp. BCC) structure.